INL/JOU-25-88065-Revision-0

Influence of Water, Vacuum, and Temperature on Surface Conditions of a Zeolite-based Molecular Sieve

July 2025

Radoslaw Zaleski, Agnieszka Kierys, Mateusz Kochel, Marcin Kusmierz, Robert Staub, Marek Wiertel, George Steven Evans, Jagoda Urban-Klaehn

Changing the World's Energy Future

INL is a U.S. Department of Energy National Laboratory operated by Battelle Energy Alliance, LLC

INL/JOU-25-88065-Revision-0

Influence of Water, Vacuum, and Temperature on Surface Conditions of a Zeolite-based Molecular Sieve

Radoslaw Zaleski, Agnieszka Kierys, Mateusz Kochel, Marcin Kusmierz, Robert Staub, Marek Wiertel, George Steven Evans, Jagoda Urban-Klaehn

July 2025

Idaho National Laboratory
Idaho Falls, Idaho 83415

http://www.inl.gov

Prepared for the
U.S. Department of Energy
Under DOE Idaho Operations Office
Contract DE-AC07-05ID14517

Influence of Water, Vacuum, and Temperature on Surface Conditions of a Zeolite-based Molecular Sieve

Radosław Zaleski, George Evans, Agnieszka Kierys, Mateusz Kochel, Marcin Kuśmierz, Jagoda Urban-Klaehn, Robert Staub, Marek Wiertel*

R. Zaleski, M. Wiertel

Institute of Physics, Maria Curie-Skłodowska University, Maria Curie-Skłodowska Square 1, 20-031 Lublin, Poland

E-mail: radek@zaleski.umcs.pl

G. Evans, J. Urban-Klaehn, R. Staub

Idaho National Laboratory, 1955 N. Fremont Avenue, Idaho Falls, ID 83415, USA

A. Kierys, M. Kuśmierz

Institute of Chemical Sciences, Maria Curie-Skłodowska University, Maria Curie-Skłodowska Square 3, 20-031 Lublin, Poland

M. Kochel

Department of Circular Economy, Institute of Energy and Fuel Processing Technology, Zamkowa 1, 41-803 Zabrze, Poland

Funding: Much of the Idaho National Laboratory portion of this work was supported by the U.S. Department of Energy, Office of Nuclear Energy, under DOE Idaho Operations Office Contract DE-AC07-051D14517 as part of the Nuclear Science User Facilities.

Keywords: commercial molecular sieves, zeolites X, positron annihilation, water adsorption, drying, beads binder

Molecular sieves such as zeolite-based materials are ubiquitous in industrial separation processes. However, there is a significant gap in understanding the surface properties and adsorption mechanisms for commercial zeolites, as most research focuses on pure zeolite powders rather than industrially relevant forms. This work addresses this gap in understanding by employing advanced characterization techniques, including positron annihilation spectroscopy, X-ray diffraction, scanning electron microscopy, X-ray fluorescence spectroscopy, X-ray photoelectron spectroscopy, liquid nitrogen sorption, and Fourier-transform infrared spectroscopy, to investigate the adsorption and desorption behavior of water in commercial zeolite 13X. Our research reveals insights into the pore-filling mechanisms, the impact of material binders on adsorption properties, and the dynamics of hydration and drying processes for zeolites. Monitoring changes on a minute scale allowed the distinction between fast and slow processes leading to sample drying. The identification of positronium bound to Na^+ ions indicated that water molecules remain in the vicinity of Na^+ ions after air-drying zeolite 13X. These findings highlight the importance of various environmental conditions in restoring zeolite properties to baseline after hydration, with significant implications for optimizing industrial processes. This work sets the direction for further research aimed at developing more efficient and robust separation techniques.

1. Introduction

Separation techniques are essential in a broad range of industrial sectors, e.g., chemical, petrochemical, pharmaceutical, and food industrial-scale production. [1] These techniques facilitate mixtures' separation, enable impurities removal, and the extraction/recovery of valuable components from raw materials. In the face of the growing challenges of environmental degradation and ongoing climate change, separation technologies are necessary to reduce the industry's impact on ecosystems, lower emissions of greenhouse gases, and close production loops within the circular economy. Further innovations in separation techniques would improve the efficiency of production processes and reduce costs, directly impacting business competitiveness, which plays a pivotal role in the global economy.

Molecular sieves, typically zeolite-based, are high-performance porous materials extensively utilized in industrial separation processes. [2-3] They are characterized by regular pore structure and a narrow pore size distribution, which enables the effect of molecular sieving. The molecular sieving process exploits differences in the size and/or shape of guest molecules relative to the diameter and shape of the pore openings of molecular sieves, enabling, among others, the separation of impurities from gas and liquid phases. Selective sieving capability combined with high microporosity, distinctive surface characteristics, and high thermal stability make these materials also invaluable in industrial adsorption and catalysis applications. [4]

Synthetic zeolite X, belonging to the FAU structure type, [5] is a commercially significant zeolite utilized in various applications. These applications include, in particular: drying processes, [6-8] natural gas purification, [9-10] CO_2 sequestration, [11-13] non-cryogenic oxygen separation methods, [14-15] removal of artificial radionuclides in nuclear wastewater, [16] and air pre-purification for cryogenic distillation. [17-18] Zeolite X, also known commercially as NaX or molecular sieve 13X, has a low SiO_2/Al_2O_3 ratio, resulting in a low-density framework with a negatively charged skeleton. This is compensated by cations, including Na^+, Li^+, K^+, and Ca^{2+}.[7, 19-20] The low silica content endows it with polar and hydrophilic properties, structural stability, and large, uniformly shaped voids, facilitating efficient adsorption.

Understanding surface properties and adsorption mechanisms in zeolites is crucial for optimizing their effectiveness in industrial processes. However, a literature review on zeolites shows significant discrepancies in the research approach. For example, Ogawa et al. [21] noted that less than 33% of academic papers concentrate on zeolites' properties and the rest on their specific applications. In addition, most research papers focus on adsorption mechanisms for pure zeolite powders; however, such powders do not fully represent more complex materials used in industrial applications. [22-25] To utilize zeolites in flow adsorption processes or catalysis, the fine powder must be converted into macroscopic forms. [26-30] This process reduces pressure drop, prevents dust formation, and improves the physical properties of the adsorbent. Moreover, the forming process can affect the adsorption capacity. [31-33] Adding binders and additives can improve the properties of the final adsorbent but also complicate the determination of its overall composition. Having complete knowledge of the composition is challenging since relevant know-how is often kept as a trade secret, making data interpretation difficult for researchers. Despite the extensive literature on zeolites, there is a need for more targeted basic research on adsorption mechanisms and surface properties using state-of-the-art methods, particularly for commercially available molecular sieves, because testing pure zeolite powders does not adequately reflect their properties. Integrating research into industry needs is essential for developing efficient processes. To fully realize the

potential of zeolites, it is necessary to conduct precise characterization under real working conditions.

Nitrogen adsorption at low temperatures is the most common method for characterizing zeolite porosity. [34] Adsorption and desorption experiments provide insights into zeolite properties by tracing pore filling and condensate evaporation. Physical sorption techniques have limitations since guest molecules may cause closed pores to open, distorting results. [35] Studies on zeolites are further complicated by the presence of defects, the influence of temperature changes, and the type of adsorbate that affects the adsorption mechanisms. The occurrence of "gating effects" (i.e., a structural variation of the adsorbent leading to a change in the gas admission) can lead to erroneous interpretation of research results. As observed by Shang et al. [36] in their seminal work, where they first described the "molecular trapdoors" mechanism, gating can significantly influence the selectivity and efficiency of adsorption, necessitating great caution in the interpretation of physical sorption results in such materials. Therefore, research on zeolites should adopt a more comprehensive approach, considering various environmental interactions affecting their porous structure and adsorption/desorption mechanisms. While numerous studies employ techniques such as physical sorption, crystallography, and microscopy to characterize NaX zeolite, better methods are necessary to observe subtle differences in pore architecture and adsorption mechanisms at sub-nanometer size.

Positron annihilation lifetime spectroscopy (PALS), and especially its variant known as positron porosimetry [37], serves as a valuable complementary technique to conventional methods for characterizing the properties of zeolites. The fundamental principle underlying PALS porosimetry is the annihilation of ortho-positronium (o-Ps), a bound state formed by an electron and a positron. o-Ps can spontaneously annihilate with its own electron, but in condensed matter, it has a high probability of annihilating with an opposite-spin electron from the pore wall. This "pick-off" phenomenon is particularly useful for assessing pore size, which can be directly calculated from the positron lifetime using a suitable quantum mechanical model for the potential well hosting o-Ps. Using this relationship and the trapping probability of o-Ps in pores of different sizes, positron porosimetry allows determining the distribution of sub-nanometer and nanometer pores. In recent years, positron porosimetry has been widely recognized as an effective approach for probing the free volumes in microporous materials, e.g., in metal-organic frameworks [38-40] or zeolites [41-45] to better understand adsorption mechanisms . [40, 46-48] PALS enables *in situ* measurements, providing real-time data of analyzed materials and the processes, to which these materials are subjected in their natural state. This enhances the reliability of results and enables precise investigation of porous materials under various external factors, such as temperature, pressure, and gas environments, without isolating the sample. This technique is highly effective for studying materials and their pores, whether they are open and interconnected or closed. Furthermore, PALS is a non-destructive technology that neither alters the material's microstructure nor influences various environmental conditions.

The presented research addresses a significant gap in the scientific literature by examining commercial zeolites, thereby enhancing both the practical and applied knowledge of these materials. PALS results could significantly improve the optimization of industrial processes utilizing zeolites by allowing lower temperatures of zeolite drying, which extends beyond the boundaries of mere academic interest.

2. Experimental

2.1 Materials

Commercial Zeolite 13X (SYLOBEAD MS 544, GRACE Davison) in the form of spherical beads with a size of 1.6-2.5 mm was obtained from ABC-Z System EKO s.c., Poland. This material will be referred to as MS13X throughout this paper. Before all experiments except the first part of the SEM and EDX measurements, the MS13X beads were powdered in a mortar. The powder was compressed into pellets using a hydraulic press for XPS, XRD, FTIR, and for the second part of the SEM and EDX measurements. For CDB measurements, samples were powdered and compressed in a separate but similar manner. An uncompressed powder sample was used for the PALS measurements, except for the samples used later in the measurements by the other mentioned methods.

2.2 Methods

X-ray diffractometry (XRD) was performed with Empyrean (Malvern Panalytical). The signals in the diffraction patterns were compared with the ICDD PDF-4+ 2023 database. The database of zeolite structures [5] was used to simulate the XRD diffractograms of hydrated and dehydrated zeolite X. Although zeolite X appears in this database under the name NaX, it corresponds to the MS13X material studied here.

Scanning electron microscopy (SEM) images were obtained using a Tescan Vega3 LMU with two detectors operating in secondary electron or backscattered electron recording mode at 20 kV or 30 kV primary beam accelerating voltage. Surface imaging was carried out for different magnifications, i.e., 200×, 2000×, 5000×, 10000×, and 20000×. The electron beam intensity used for imaging gave a spot size on the sample surface in the range of 280 nm to 60 nm for 200× and 10000×, respectively.

X-ray fluorescence spectrometer (EDX) from Oxford Instruments, coupled to Tescan Vega3 LMU, was used for X-ray microanalysis. The EDX spectrometer was equipped with an X-act SSD semiconductor detector with an active area of 10 mm^2, operating at room temperature with the energy resolution of approximately 125 eV at 5.9 keV, the Mn K_α line. The spectrometer was operated using AZtecEnergy analytical software.

The X-ray Photoelectron Spectroscopy (XPS) measurements were performed using a hemispherical Scienta R4000 electron analyzer equipped with the X-ray source (Scienta SAX-100, Al K_α, 1486.6 eV, 0.8 eV band) and the XM 650 X-Ray Monochromator (0.2 eV band). The X-ray source operating parameters were as follows: U = 15 kV, I_e = 10 mA. The pass energy of the analyzer was set to 200 eV for survey spectra (with 750 meV steps) and 50-100 meV for regions (high-resolution spectra): Al 2p, Si 2p, Mg 2p, O 1s, C 1s, Na 1s. The base pressure in the analysis chamber was $5 \cdot 10^{-9}$ mbar (ultra-high vacuum conditions), and it did not exceed $3 \cdot 10^{-8}$ mbar during spectra collection. Shirley-type background subtraction followed by Gauss-Lorentz curve fitting was performed to analyze the raw peaks.

Nitrogen adsorption and desorption measurements were performed at a cryogenic temperature of 77 K on an ASAP 2020 (V4.01 J) volumetric adsorption analyzer (Micromeritics, Norcross, GA) equipped with a turbo vacuum pump capable of reducing the pressure to below 10^{-7} Torr. Before measurement, the sample was degassed at 120 °C for 17 hours. The standard Braunauer-Emmett-Teller (BET) equation [49] was used to calculate the specific surface area, S_{BET}. The total pore volume V_p was estimated from single-point adsorption at a relative pressure of approximately 0.997. The micropore area, the external surface area, and the micropore volume were estimated from the t-plot. The pore size distribution (PSD) was obtained from the Density Functional Theory (DFT) model in the Micromeritics MicroActive

v1.01 software package, taking into account the following assumptions: (1) the nitrogen adsorption - DFT model and the slit pore shape; (2) the nitrogen adsorption - DFT model and the cylindrical pore shape.

A custom digital spectrometer was used for the positron annihilation lifetime spectroscopy (PALS) analysis. Agilent U1065A (formerly known as DC252) digitizers were used to collect signals from two detectors equipped with Ø1.5"×1" BaF_2 scintillators and Hamamatsu R3377 photomultipliers. The detectors were mounted in the immediate vicinity of the sample chamber. The digitizers, with a sampling rate of 4 GS/s, were triggered with a dedicated fast coincidence unit. The positron lifetime spectra were generated in flight from digitized impulses using an algorithm developed by the Prague group [50]. The time range of the digital spectrometer was 2 μs.

The water adsorption/desorption measurement was carried out using a chamber specially designed for PALS measurements in a controlled atmosphere [47]. As received, the powdered **Fresh** MS13X sample (T-1 in Appendix 1) was placed in a loosely capped container in the sandwich configuration (sample-positron source-sample). A positron source (^{22}Na) with activity of 300 kBq was used. The sample was heated to 473 K under vacuum $p < 10^{-4}$ Pa until no change in positron spectra was observed (33 h). Mili-Q water (18.2 MΩ cm at 298 K) was outgassed three times by freezing, pumping, and thawing cycles. The vessel containing the water was connected to the chamber through a Pfeiffer EVR 116 gas dosing valve. The vapor flow was regulated using a Pfeiffer RVC controller. In 20-300 Pa steps, the water vapor pressure in the chamber was increased to the saturated vapor pressure (relative pressure of 100%) and then lowered to a high vacuum. A positron annihilation lifetime spectrum was collected for 6 h when the vapor pressure stabilized after each change. All sorption measurements were performed at 21-22 ºC (stabilized by air conditioning).

The positron annihilation lifetime (PAL) spectra acquired during other than sorption measurements were collected using a 100 kBq positron source, ensuring a low background, which allowed for an accurate analysis of long-lived components. The data were saved at every ca. 28-32 minutes (a total number of counts of ca. 0.2 million) to explore the dynamics of processes occurring during heating and/or pumping. PAL spectra integrated over the entire acquisition time, i.e., 24-hour data with a total number of counts of ca. 10 million, were used for more detailed numerical analyses.

The LT program [51] was used to decompose the 10 million positron lifetime spectra from all measurements into three to six discrete components. Alternatively, the MELT program [52] provided continuous lifetime distributions, which were transformed to pore size distributions using positron porosimetry equations assuming cylindrical pore shape [37]. A single Gaussian with FWHM of ca. 206 ps and 200 ps sufficiently approximated the resolution curve for 100 kBq and 300 kBq sources, respectively.

Coincidence Doppler Broadening (CDB) measurements and simultaneous PALS control were performed using the DPALMS-LCA system (TechnoAP, Japan) [53]. A pair of BaF_2 scintillators and Hamamatsu H3378 photomultipliers were used for PALS, while a pair of ORTEC GEM15P4 HPGe detectors were used for CDB. ^{22}Na positron source with activity of 550 kBq was used. The CDB results were analyzed with the CDB-AP software [54]. The energy resolution at the annihilation line (511 keV) was 1.17 keV. Control PAL spectra with ca. 10 million counts had a time resolution with FWHM of ca. 204 ps.

For each measurement of zeolite samples, several pellets (usually three) were heated for 24 hours at 120 °C in a vacuum (**Fresh-dry vac 120 °C,** T-2 in Appendix 1) or the air (**Fresh-dry air 120 °C**, T-3 in Appendix 1). Then the samples were rehydrated in the air at a

humidity of ca. 40% and labeled **Fresh-dry vac 120 °C-hydr** and **Fresh-dry air 120 °C-hydr** (T-11 and T-12 in Appendix 1, respectively), as confirmed later by PALS results. The two most robust pellets were quickly placed in the sandwich configuration (sample-positron source-sample) around a Na-22 positron source and vacuum-sealed into a bag. Simultaneous CDB and PALS measurements on the samples began shortly after tightly sealing samples. Reference samples were also measured using simultaneous CDB and PALS: sapphire (alumina) and quartz (silica) for comparison. These samples were sandwiched around the Na-22 positron source and placed in approximately the same position as the zeolite samples, but without the vacuum-sealed bag.

3. Results and discussion

3.1 Characterization

The commercial molecular sieve (MS13X) was characterized before its hydration (**Fresh**, T-1 in SI, Appendix 1). The main component of MS13X is faujasite (FAU zeolite framework type, Fig.1a), as indicated by the X-ray Diffraction (XRD) patterns (SI, Appendix 2). Energy Dispersive X-ray Fluorescence Spectroscopy (EDX) analysis (SI, Appendix 4) points to a low-silica form of faujasite, i.e., zeolite X. In contrast, X-ray Photoelectron Spectroscopy (XPS) shows a twice as high Si to Al ratio (SI, Appendix 5). This discrepancy is easily explained by noting that Si is not only a component of the MS13X aluminosilicate crystallites but also a component of the binder, which is shown by EDX studies (SI, Appendix 4, Fig.S5). The Scanning Electron Microscopy (SEM) micrograph of the interior of the cracked MS13X bead (Fig.1b) reveals that the binder takes the form of subtle spiderweb-like fibers. Meanwhile, on the surface of the MS13X beads, the presence of the binder, which is in a more granular form, is even more pronounced (SI, Appendix 3). Since XPS provides information about a surface layer of ca. 5 nm thickness, the binder, regardless of its form, constitutes a surface that is exclusively accessible for XPS analysis. The penetration depth of EDX is over a hundred times greater, providing information that is much more proportional to the binder-to-zeolite ratio in the depth of the material.

The EDX analysis shows that of the three common forms of synthetic faujasite (faujasite-Na, faujasite-Ca, or faujasite-Mg), the molecular sieve is NaX zeolite. Although Mg (along with C and Fe) is also present in a small amount on the surface exposed after crushing the MS13X beads (SI, Appendix 4, Fig.S5 and S6), its location suggests that it is a part of the binder that the manufacturer used to form the molecular sieve into beads. Once again, XPS gives a different Na to Mg ratio compared to EDX, with XPS indicating a predominance of Mg. However, the XPS measurement only confirms the location of Mg in the binder, which surrounds the crystallites.

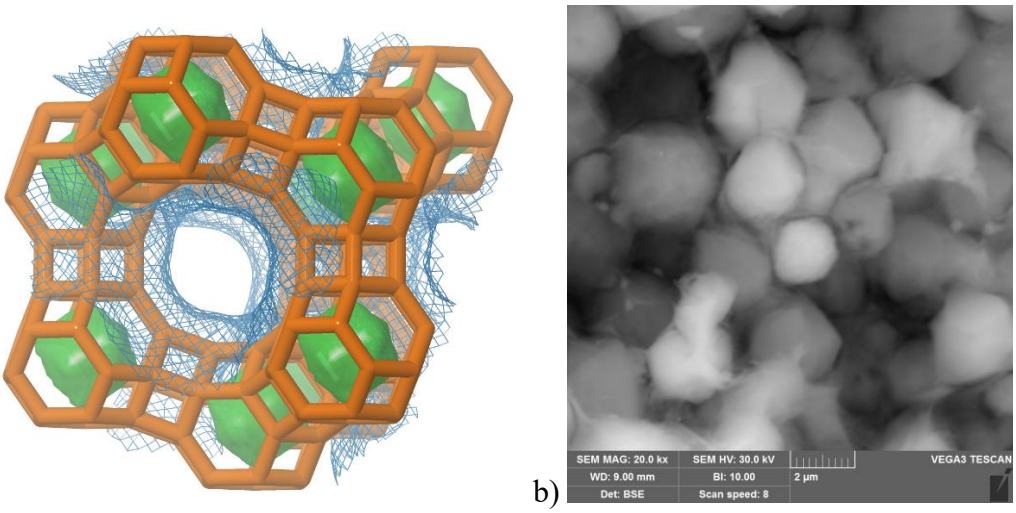

Fig.1. (a) Framework type FAU (supercages are marked in blue, while sodalite cages are marked in green); [5] (b) SEM micrograph of the interior of the cracked bead of MS13X.

Nitrogen adsorption and desorption measurements indicate a predominant contribution of micropores to the high porosity of MS13X (SI, Appendix 6). The pore size distribution obtained by the Density Functional Theory (DFT) method with an assumption of the cylindrical shape of pores shows a single narrow and well-resolved peak with the maximum located at a diameter of 0.77 nm, which is in surprisingly good agreement (as for methods based on very different principles) with the size of 0.78 nm obtained from the positron porosimetry assuming the same pore shape (Fig.2**,** Table 1). These results are in agreement with the maximum size of the sphere that can diffuse along the FAU framework supercages, i.e., 0.735 nm. [5] However, the assumption of the cylindrical shape of pores in the DFT model does not seem appropriate for meso- and macropores since it results in a questionable single-point peak at the end of the range (Fig.2, blue). The model that assumes a slit shape is much more realistic for these large intracrystallite spaces, which confirms a more reliable result, i.e., a very wide range of sizes with a wide maximum at around 40 nm. In contrast, the slit model does not fit supercages since their shape is clearly different, as it is known from the faujasite crystalline structure (Fig.1a).

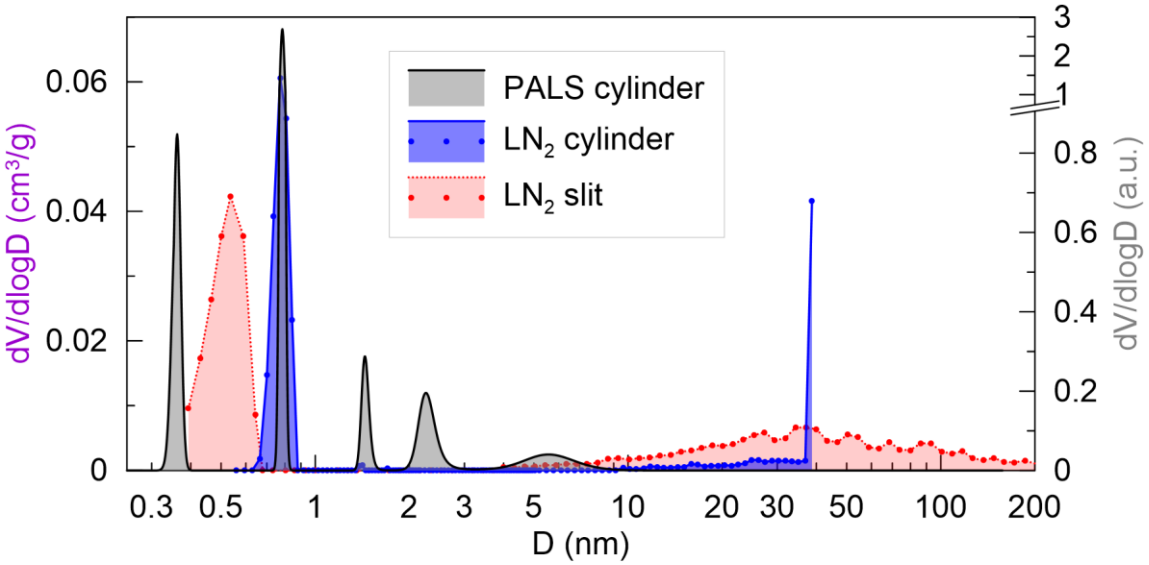

Fig.2. Pore size distributions in zeolite-based molecular sieve from PALS (determined using positron porosimetry from MELT results, assuming the same pore shape) and from LN2 adsorption/desorption (determined by the DFT method, assuming cylindrical or slit pore shapes).

Table 1. Mean pore size, full width at half maximum of pore size distribution, and relative pore volume (area under PSD peaks) calculated using positron porosimetry equations from MELT results, assuming the cylindrical pore shape. Sample names and numbers refer to the treatment method in SI, Appendix 1.

D_{mean} (nm)	FWHM (nm)	Volume (arb. unit)
Fresh-dry vac 120 °C (T-2)		
0.36	0.02	63
0.78	0.03	112
1.45	0.09	20
2.28	0.31	31
5.26	2.39	19
Hydr-dry vac 20 °C (T-5)		
0.42	0.02	36
0.77	0.04	161
1.05	0.04	4
13.22	6.72	4
Hydr-dry vac 120 °C (T-6)		
0.36	0.03	59
0.78	0.04	111
1.31	0.11	17
2.15	0.31	34
4.89	2.61	21
Hydr-dry air 120 °C (T-7)		
0.37	0.04	77
0.76	0.08	96
1.15	0.20	15
2.09	0.59	5

Positron porosimetry, besides exceptionally good agreement in the size of supercages (0.78 nm), shows four other peaks in the pore size distribution. The smallest free volume peak at 0.36 nm is below the size range detectable by nitrogen sorption. It can be ascribed to the free volume of sodalite cages [5] (green shape in Fig.1a). The largest pores with size within the range of 4-10 nm are most likely the tail of the wide distribution of intracrystallite space sizes, which PALS only detects in lower-sizes range due to its poor sensitivity to large pores. The origin of free volume with a size of 1-3 nm is more challenging to pinpoint. These are likely to be closed pores because otherwise, they would be detected by nitrogen sorption . Hence, any location in contact with highly interconnected supercages is excluded. It is also unlikely that they are located in the MS13X's binder, as they constitute more than 20% of the total free volume in MS13X (Table 1). Since the binder mass (including the unknown Si mass fraction) from the EDX results accounts for less than 10% of the total mass, this would suggest that the binder is twice as porous as the zeolite, which is highly unlikely. Therefore, the most probable explanation points to the annihilation of ortho-positronium (o-Ps) being chemically bonded to the pore surface (supported later in the text), instead of o-Ps trapped in pores, as typically assumed. In that case, the peaks in the range of 1-3 nm would have to be excluded from the regular MS13X pore size distribution.

3.2 Water adsorption and desorption

3.2.1 Adsorption

PALS is an excellent technique for *in situ* monitoring of porosity changes during adsorption and desorption of various substances, [46, 55-59] including water, [40, 47, 60] in different types of rigid and polymeric frameworks. Also, for MS13X, PALS enables highly accurate monitoring of water adsorption and desorption processes if the lifetime distributions are approximated by mean lifetime values (τ_n). The two short-lived components (n = 1, 2, see SI, Appendix 7, Fig.S9) are not sensitive enough to be useful for open volume monitoring; therefore, only four long-lived components (n = 4-6) related to o-Ps annihilation (Fig.3) are discussed further. In MS13X before water adsorption (**Fresh**, T-1 in SI, Appendix 1), the origin of each of the four components with different mean lifetimes can be assigned to different free volumes. These are free volumes in sodalite cages (n = 3), free volumes in supercages (n = 4), and intercrystallite free volumes (n = 6). The origin of the fifth component (n = 5) is uncertain, and perhaps it can be assigned to the chemically bound o-Ps. At the very beginning of water absorption, below the relative water pressure ($p_r = p/p_0$, where p_0 is water saturated vapor pressure) of ca. 7% (stage I, Fig.3), no changes in the mean lifetimes and intensities of o-Ps components are observed. The first stage of adsorption is observed in the range of p_r = 7-17% (stage II, Fig.3), with a significant decrease in the I_4 intensity (by ca. 5%) only. This indicates that the water blocks a part of the pore surface where positronium could have previously formed. The lack of decrease in τ_4 below the relative pressure of 25% indicates that water molecules do not fill up the space inside MS13X supercages even partially. Because it is implausible that water blocks supercages fully or not at all, openings of supercages are the most probable location of water at stage II, i.e., connections between them or with the outside of the crystallites.

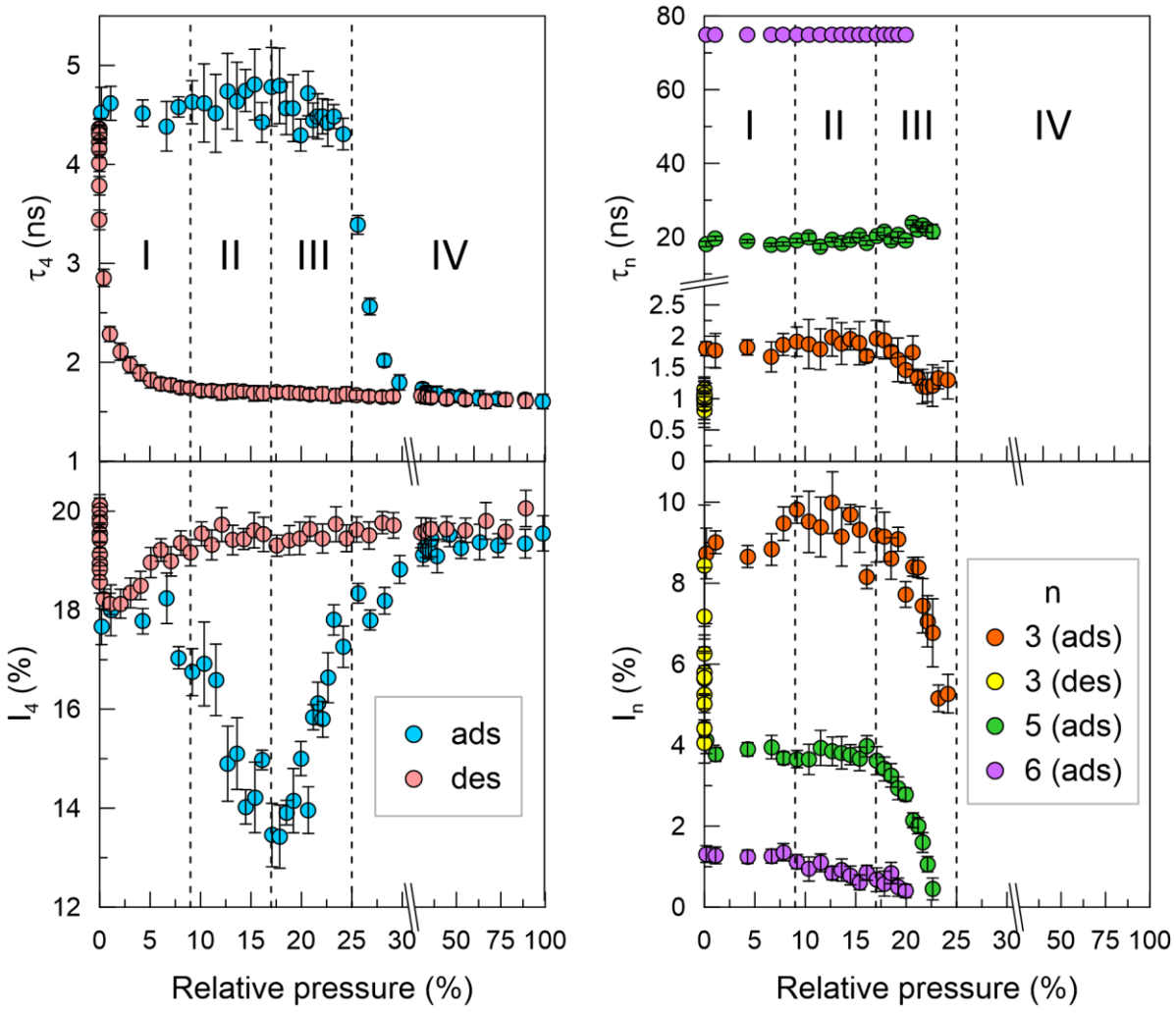

Fig.3. Lifetimes (τ) and intensities (I) of o-Ps components determined by LT as a function of relative water vapor pressure during its adsorption and desorption from MS13X. Components 5 and 6 are not observed during desorption.

The next stage (III in Fig.3) of adsorption can be identified in a relative pressure range between p_r = 17% and 25%. In this range, the intensities (I_3, I_5, and I_6) of all o-Ps components except the one related to the supercages (I_4) decrease until they disappear completely. The simplest explanation is that at p_r = 25%, all free spaces other than the supercages are filled with water. However, this is reasonable only in the case of sodalite cages, which are smaller than the supercages. Larger pores of several nanometers in size (e.g., intercrystallite spaces) should still be opened at a much higher pressure, which was also observed by PALS. [47] This confirms that the fifth component is unlikely to represent a group of pores with a size of ca. 2 nm because, in this case, it should not disappear until p_r reaches about 40%. Also, the sixth component, which represents intercrystallite-free volumes, should remain unaffected until p_r of about 80% according to the Kelvin equation (this is confirmed by unpublished PALS measurements for SBA-15). Instead, I_6 gradually decreases from p_r = 7%, the same relative pressure as when I_4 began decreasing (reflecting the relative number of o-Ps that annihilate in much smaller free volumes of the supercages). This indicates that the main contribution to I_6 comes from a commonly observed phenomenon of o-Ps migration from intragranular supercages to intergranular spaces. [61] This process has a relatively low yield in MS13X due to the small size of supercages and large grains, which results in I_6 < 1.3% only. The migration probability decreases with an increasing degree of supercage blocked by water

molecules accompanying the increase in p_r; therefore, when $p_r > 20\%$, the sixth component becomes indistinguishable from the background. Unlike the intensity of the other components, I_4 increases from ca. 13% to 19% (i.e., by almost 6%) at stage III. Some of this is a normalization effect due to the relative nature of intensities – a 15% decrease in $I_3+I_5+I_6$ is compensated by an increase in I_4. However, it is also possible that, in addition to the formation of o-Ps using electrons from the supercage walls, some o-Ps are formed using electrons from water molecules blocking the supercage openings, resulting in this fraction of o-Ps contributing to the increase in I_4.

The final adsorption stage (IV) starts with p_r at about 25% and applies to the fourth component only. The corresponding o-Ps lifetime τ_4 decreases rapidly from 4.6 ns to 1.7 ns with increasing pressure, showing a sharp decrease in the size of the free volumes in the supercages. This is a consequence of filling the supercages with water molecules. It has been previously reported that o-Ps can repel molecules forming a bubble in bulk water (or other liquid), [62] as well as water confined in pores, even with nanometer-sized pores. [47] The typical lifetime in the bubble is about 1.84 ns, [63] but after water adsorption in MS13X, the τ_4 lifetime decreases to 1.7 ns, and at $p_r = 100\%$, it lowers to 1.6 ns. This discrepancy is not surprising considering that lifetimes in the range 1.76-2.62 ns were observed at room temperature for positrons annihilating in confined water in various porous materials [47, 64-71]. Since usually an increase in lifetime was observed in these complex systems our result requires explanation as given below. Reduction of τ_4 below 1.84 ns in MS13X may have a twofold origin: (1) restriction in the movement of water molecules in the supercages and/or (2) o-Ps interaction with both water molecules and walls of the supercages. The small reduction in τ_4 from 1.7 ns to 1.6 ns in the p_r range of 30-100% is caused by increasing liquid pressure in the supercages in response to the change of the outside vapor pressure [46] and confirms that o-Ps repels water molecules, which offer more resistance at higher pressure.

The detailed analysis of pore size distributions (Fig.4) shows that the component remaining in the MS13X after water adsorption (**Hydr vac**, T-4 in SI, Appendix 1) has a bimodal nature with maxima at about 0.4 nm and 0.5 nm. The free volume of a larger size (FV_L in Fig.4) can be attributed to the remaining empty space within the supercages. In the final stage IV of water adsorption, i.e., at $p_r = 25$-30%, this free volume is systematically shrinking (SI, Appendix 7, Fig.S10). On the other hand, the free volume with a smaller size (FV_S in Fig.4) is most likely the space created by o-Ps repelling water molecules. This peak overlaps with the one ascribed to sodalite cages in dry MS13X, but a gradual decrease in its intensity was observed at stage III of adsorption (Fig.3), so this annihilation process is expected to have a minor contribution in the hydrated MS13X.

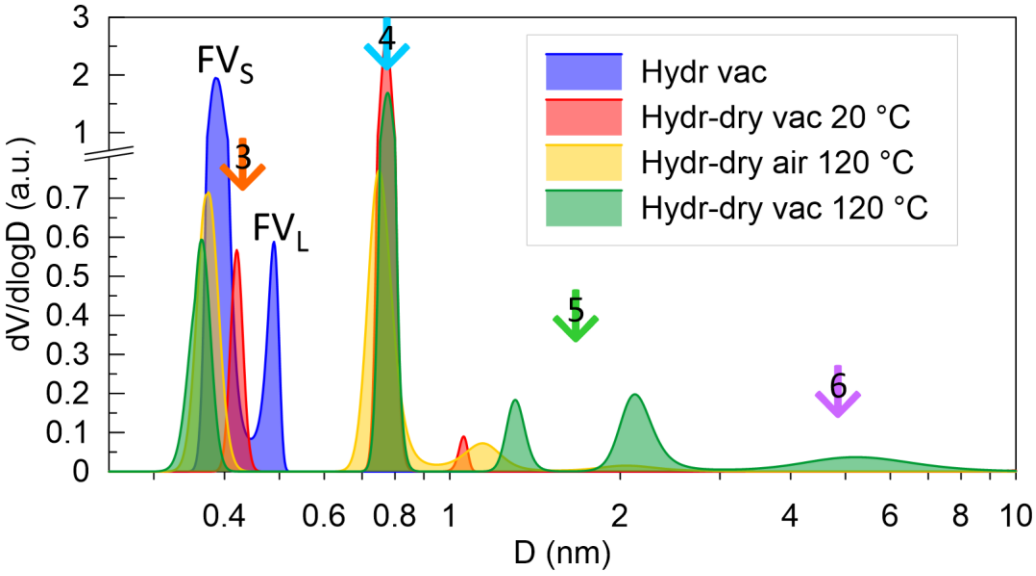

Fig.4. Pore size distributions measured at 20 °C by positron porosimetry from MELT results assuming cylindrical pore shape in MS13X – hydrated (**Hydr vac**) and dried after full hydration in various conditions: vacuum at 20 °C (**Hydr-dry vac 20 °C**), air at 120 °C (**Hydr-dry air 120 °C**), or vacuum at 120 °C (**Hydr-dry vac 120 °C**). Arrows indicate sizes corresponding to the lifetimes τ_3-τ_6 presented in Fig.3 at zero relative pressure before adsorption.

3.2.2 Desorption

The course of desorption is completely different from that of adsorption with a pronounced hysteresis loop (Fig.3). First of all, the fifth and sixth o-Ps components do not appear at all during water desorption, while the third one appears only when the water vapor pressure reaches almost zero. As for the fourth o-Ps component, no change in I_4 is observed in the p_r range from 100% to nearly 5%, while τ_4 increases slowly from 1.6 ns to over 1.7 ns due to the reduction in liquid pressure. Below p_r = 5% the increase in τ_4 speeds up until it reaches a value of 4.5 ns at zero pressure. In the same range, I_4 decreases slightly, and then, when the vacuum pump is turned on, it starts to increase (Fig.5). The shape of this change resembles the I_4 pressure dependence during adsorption in the range of 18-30% and might also have a similar (although opposite) origin, i.e., loss of water molecules, that serve as o-Ps forming sites. A much smaller total decrease during desorption than the increase during adsorption can be explained by a lack of changes related to the relative character of the intensities (no other components appear), which was a factor influencing I_4 in the case of adsorption.

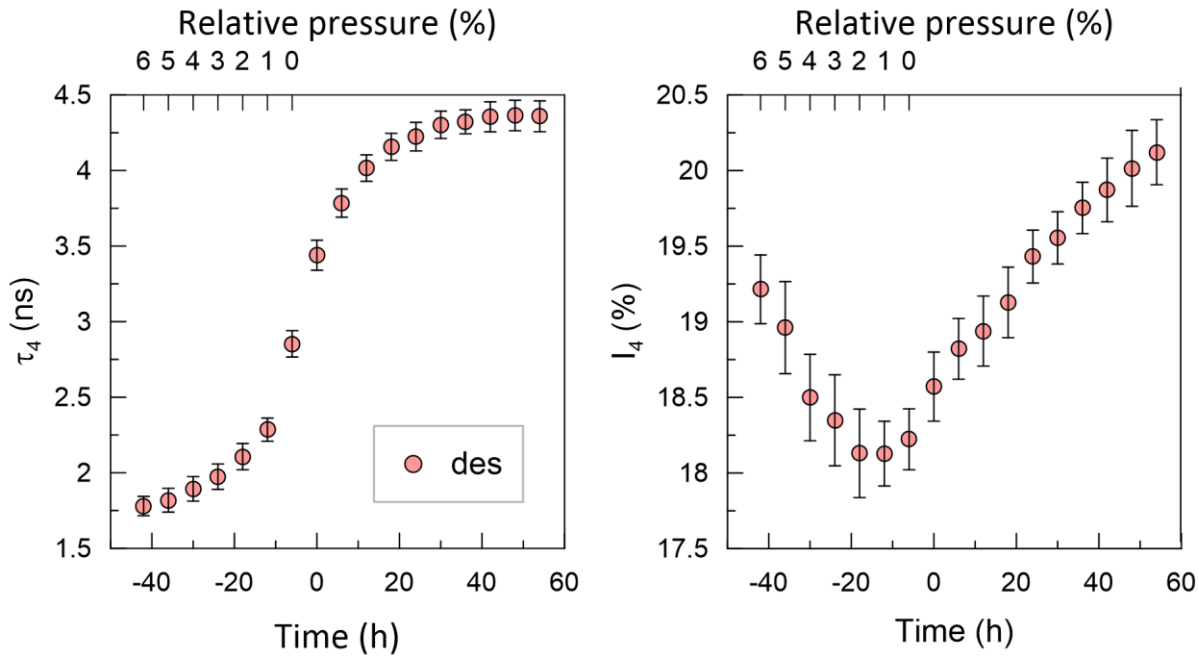

Fig.5. Lifetime (τ_4) and intensity (I_4) of the single ortho-positronium component determined by LT averaging both, supercage and solidate cage components in MS13X as a function of relative water vapor pressure during the last phase of desorption that results in obtaining **Hydr-dry vac 20 °C** (T-5 in Appendix 1). Time zero is the beginning of continuous pumping.

The final desorption stage occurs when MS13X is held at almost zero pressure, i.e., in a vacuum obtained with a turbo pump (Fig.5). The lifetime τ_4 stabilizes after about 30 hours but does not reach the value of 4.6 ns, observed before adsorption. The intensity I_4 recovers even more slowly – it does not reach saturation even 60 hours after the beginning of continuous pumping. It should be emphasized that, in parallel with the stabilization of the fourth component in the vacuum, the third component is eventually restored but has a significantly lower lifetime (Fig.3). This lifetime reduction may indicate that water remains in sodalite cages. In contrast, the fifth and sixth components do not appear at all. (Fig.4, Table 1) shows that in the sample treated analogously as during the adsorption-desorption cycle, i.e., **Hydr-dry vac 20 °C** (T4 in SI Appendix 1), only four free volume groups exist with maxima at about 0.4 nm, 0.8 nm, 1 nm (negligibly small peak) and 13 nm (a very wide distribution). This indicates that the initial state of the MS13X, observed in the **Fresh** sample, cannot be restored after drying in a vacuum at room temperature.

To restore the hydrated MS13X (i.e., exposed to saturated water vapor for ca. 24 hours) to its initial state, it was decided to dry it first in the air at 120 °C for about 24 hours, but the result was relatively modest (Fig.4, Table 1). In the resulting sample, named **Hydr-dry air 120 °C** (T6 in SI Appendix 1), the volume of the sodalite cage component (~0.4 nm) increased significantly at the expense of the supercage component (~0.8 nm), but the range of larger free volumes increased noticeably only around 1 nm in comparison to the **Hydr-dry vac 20 °C** sample (Fig.4, Table 1). Surprisingly, heating hydrated MS13X at just 120 °C in a vacuum efficiently restored the initial state of the sample, i.e., **Fresh**. However, the sample's state takes many hours to stabilize, even in this case. Overall, this shows that to discover how water interacts with zeolite, it is crucial to understand how hydration and heating in air and vacuum influence the state of the system. For this purpose, it would be best to monitor the course of these processes, as presented in the next chapter.

3.3 Drying dynamics

Although the acquisition of statistically significant spectra that allow to separate components with sufficient accuracy requires a few to a dozen hours, it is possible to monitor relative changes on the scale of minutes. This is done by choosing appropriate time ranges in the spectra and integrating the number of counts in these ranges. Two ranges were chosen (Fig.6), which cover counts representing o-Ps annihilations in (A) both supercages and large pores with D > 1 nm (components numbered by n = 4, 5, 6) and (B) large pores only (n = 5, 6). The o-Ps counts in the short time range (left from A and B ranges) are related to o-Ps annihilation in water (and, unfortunately, also in sodalite cages, which cannot be separated from water). It is also impossible to separate contributions from distinct components in range A, so the changes are more clearly interpreted using their sum (A+B) and ratio (A/B). The number of counts in A and B depends on both lifetimes and intensities, but treatments that cause changes in intensities do not change lifetimes substantially. With this assumption, the change in A+B reflects the change in total pore volume, while A/B reflects the change in the volume of MS13X supercages relative to the volume of large pores.

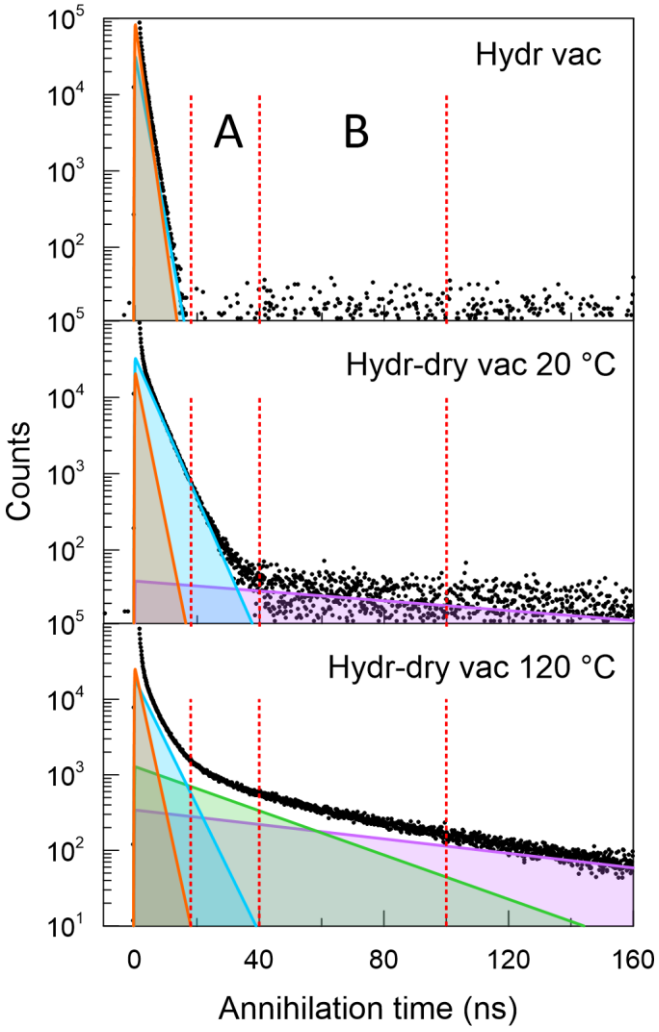

Fig.6. PAL spectra at 20 °C of MS13X with pores filled with water (**Hydr vac**) or dried in a vacuum at 20 °C (**Hydr-dry vac 20 °C**) or 120 °C (**Hydr-dry vac 120 °C**). Components 3-6, presented in Fig.3, are marked with corresponding colors. Red dashed lines separate the two time intervals used for calculating the sums of counts A and B.

Tracking changes during the hydration and drying of MS13X samples becomes possible using the A+B and A/B parameters. The hydration process occurs relatively quickly, regardless of the prior sample treatment (SI, Appendix 7, Fig.S11). About 90% of the changes in both parameters occur within half an hour. However, in addition to fast water physisorption, there is an additional slow relaxation process that lasts 4-5 hours. This can be related to the reorganization of water molecules in MS13X, possibly due to the formation of bonds with zeolite.

Vacuum drying of the samples starts with opening the valve to the vacuum pump and, optionally, turning on the heater. After that, the temperature and vacuum stabilize within 10-20 min. The sums of counts A and B collected every 19 minutes show an increase in free volume in both all pores (A+B) and supercages (A/B) with evacuation time (Fig.7). The difference between the initial (time zero) values of the relative supercage volume (A/B) most likely reflects the change of the ratio $I_4/(I_5+I_6)$ with temperature, which is shown in SI Appendix 7, Fig.S12. Although the increase rate in A/B varies moderately with temperature, it does not show a clear relationship. In contrast, the rise in A+B depends significantly on the heat applied during evacuation.

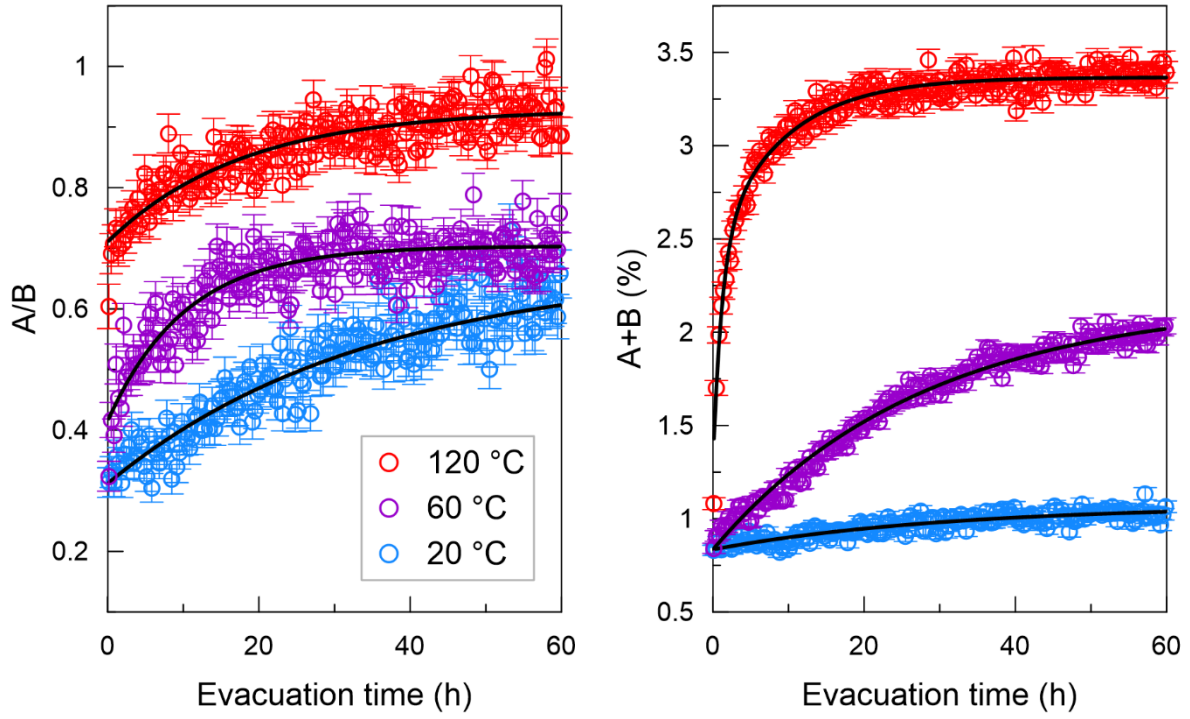

Fig.7. Counts sum (A+B) and ratio (A/B) in time windows A (18-40 ns) and B (40-100 ns) of PAL spectra collected during removing water from hydrated MS13X (**Hydr vac**, T-4 in Appendix 1) at various temperatures. Regression lines are exponential functions fitted to experimental data.

To compare the results of different treatments, the untreated sample served as a reference (**Fresh**). Even after its storage in the sealed bottle for an unknown period since production, it was already fully hydrated, which is not surprising, taking into account the low humidity (~30%) required to fill MS13X supercages (Fig.3). For comparison, two samples were used:

1. hydrated, then dried in a vacuum at 20 °C (**Hydr-dry vac 20 °C**) and rehydrated in a vacuum again (labeled as **Hydr-dry vac 20 °C-hydr**),
2. hydrated, then dried in the air at 120 °C (**Hydr-dry air 120 °C**) and rehydrated in a vacuum again (labeled as **Hydr-dry air 120 °C-hydr**).

The 28-minute steps were chosen to track heating effects over time. This was a compromise between the ability to observe rapid changes and the reduction of uncertainty for small and slow changes. The course of heating at 120 °C depends clearly on the sample treatment (Fig.8). The most pronounced differences are observed in the total pore volume increase (SI, Appendix 7, Table S5, the parameters ΔN_1+ΔN_2, N_{max} of A+B). The N_{max} of A+B for the air-dried (**Hydr-dry air 120 °C**) sample (1.56%) is about 0.4 of the N_{max} of A+B of the **Fresh** sample (2.67%), as opposed to the N_{max} of A+B of the vacuum-dried (**Hydr-dry vac 20 °C**) sample (3.24%), which was about 1.2 of that of the fresh sample. Conversely, the upper limit of the relative supercage volume (A/B) is the largest for the air-dried sample, followed by the fresh sample, and the smallest for the vacuum-dried sample. The differences in the upper limit for A/B are much smaller than for A+B. Still, they show that in the air-dried sample, the additional volume comes almost exclusively from the further removal of water from supercages, not the larger pores. This further deepens the differences in the contribution of individual pore fractions observed at room temperature before rehydrating (Table 1).

The initial very fast change in A/B occurs during the first 20 minutes of increasing temperature (Fig.8). This initial step can be noticed only at elevated drying temperatures (Fig.7), which proves that it is driven by the difference between PALS results at 20 °C and 120 °C (SI, Appendix 7, Fig.S13). The further changes in A/B are on the order of hours, and they are twice as slow for the vacuum-dried sample compared to the air-dried sample (SI, Appendix 7, Table S4, the time constant T_1). The time constants of the increase in A+B and A/B do not match, indicating that free volumes in supercages and larger pores develop at different rates during heating and are probably driven by distinct processes. A fast process (time constant of 1-2 hours, first stage) common for all samples may reflect the removal of weakly bound water present in all free spaces. In the second stage, a slow process (time constant of 6-11 hours) is observed only for fresh and vacuum-dried samples. However, it is faster than the change in A/B, which means that the volume in larger pores stabilizes faster than in supercages.

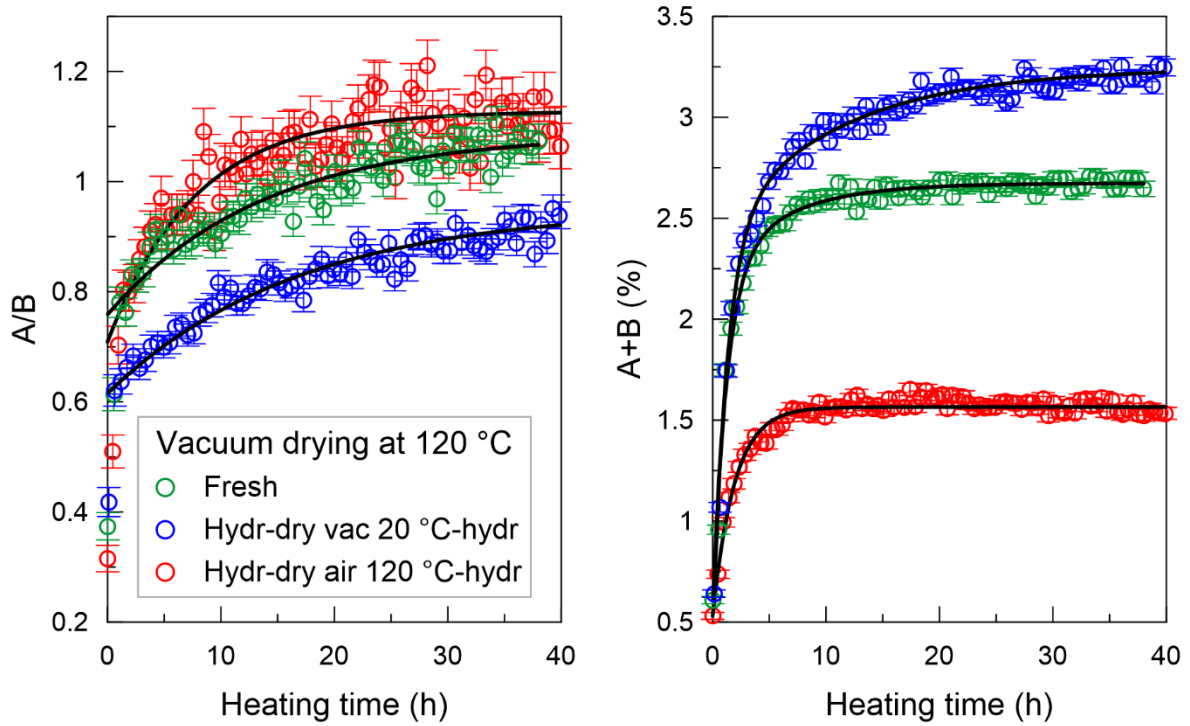

Fig.8. Counts sum (A+B) and ratio (A/B) in selected time windows of PAL spectra collected during heating in a vacuum at 120 °C for MS13X samples: untreated reference (**Fresh**); hydrated, then dried in a vacuum at 20 °C and rehydrated in a vacuum (**Hydr-dry vac 20 °C-hydr**); hydrated, then dried in the air at 120 °C and rehydrated in a vacuum (**Hydr-dry air 120 °C-hydr**).

The most straightforward interpretation of the time changes in PAL spectra leads to the conclusion that samples' hydration generates additional free spaces with a size of a few nanometers. However, this should lead to a change in the MS13X structure, which is not detected by XRD (SI, Appendix 2, Fig.S1). Therefore, either these free volumes exist permanently in the MS13X structure and are blocked in the air-dried sample (and in the fresh sample to a lesser extent), or they are a misinterpreted result of an additional effect accompanying o-Ps annihilation. We will consider both possibilities.

The pores could be blocked by water or the major components of air, namely nitrogen or oxygen. First, we will focus on this second possibility. It is quite unlikely that nitrogen or oxygen is physisorbed in the amount sufficient to block the pores larger than MS13X supercages. Nitrogen or oxygen adsorption was detected in the smallest pores of SBA-15, whose size is comparable to that of the cages in MS13X, and it was a very slow adsorption process. [72] Despite the adsorption process being slow, the adsorbed gases are quickly removed from the pores in a vacuum. Additionally, if oxygen was adsorbed, it would reduce o-Ps lifetimes due to ortho-para conversion. Water is more likely than air to be a blocking agent, and water is present in pores in large amounts when a sample begins to be heated in the air. The Fourier-Transform Infrared Spectroscopy (FTIR) wide band at 3000-3600 cm^{-1} (Fig.9), which corresponds to O-H vibrations in water, confirms that water is present in significantly larger quantities in air-dried MS13X compared to the other samples.

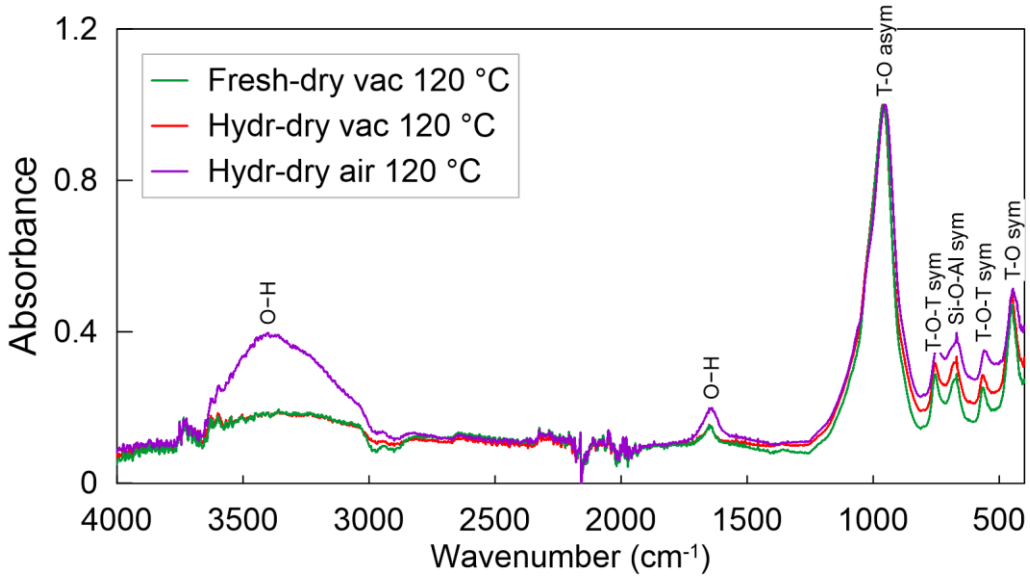

Fig.9. FTIR spectra of MS13X without any treatment dried at 120 °C in a vacuum (**Fresh-dry vac 120 °C**) or hydrated (pores filled with water) MS13X that was then dried at 120 °C in either a vacuum (**Hydr-dry vac 120 °C**) or in the air (**Hydr-dry air 120 °C**).

3.4 Water binding

It is essential to stress that the condition of the sample obtained by heating in a vacuum at 120 °C remains unchanged even though it is exposed to air at room temperature (SI, Appendix 7, Fig.S13). So, the elevated temperature (up to 120 °C in our study) is necessary to achieve a permanent change, which we observe as the disappearance of long-lived o-Ps components. This is an argument against physisorption, which is more efficient at low temperatures. On the contrary, it implies that the effect can be a result of a thermally initiated chemical reaction involving oxygen or carbon dioxide. The observed difference between heating the hydrated (**Hydr-dry vac 120 °C**) and air-dried (**Hydr-dry air 120 °C**) samples at 120 °C in a vacuum indicates that water bonds more strongly in the latter case. So far, only "mobile" water has been observed in zeolite 13X. [73] Moreover, the FTIR spectra do not show double bands centered at 2500 cm^{-1} and 2900 cm^{-1}, characteristic of water H-bonded to Brønsted acid sites. [74] Therefore, the water must be strongly bound to another site to withstand heating at 120 °C in a vacuum. The exchangeable cations create suitable sites for forming strong interactions with highly polar water molecules. [75]

The alternative explanation is that the lifetimes in the range of 10-50 ns, typically interpreted as o-Ps annihilation in the pores with a size of 1-3 nm, are unrelated to real free volumes. Chemical bonding to atoms can significantly influence the o-Ps annihilation rate, [76-78] although it is usually disregarded. The energy of such bonds is high enough (a few tenths to one eV) that they are not thermally broken at the temperatures used in this study. The lifetime calculated for the PsH (positronium hydride) molecule is of an order of 1 ns, which is smaller than the lifetimes considered in our study. However, it cannot be ignored that binding to other atoms in the zeolite environment can result in significantly larger lifetimes. An intriguing possibility is the formation of the $PsNa^+$ complex. [79]

The consideration that water binds and fills empty spaces is also valid for the explanation based on forming the Ps-atom complex; however, in this case, we expect a smaller number of water molecules populating Ps-binding reaction centers instead of filling empty spaces. This argument is supported by the results of Coincidence Doppler Broadening (CDB) spectroscopy (SI, Appendix 8). In the rehydrated samples, over 70% of positrons annihilated without

forming positronium. Most of these positrons find local potential wells where they can localize weakly bonding to functional groups that have some affinity to positively charged particles, and eventually annihilate. The lifetime of these positrons (labeled "non-Ps") is shorter than 1 ns, thus less sensitive to different positron annihilation sites compared to o-Ps pick-off annihilation. If a change in the lifetime (such as from ca. 560 ± 40 ps to 400 ± 30 ps during water adsorption) is accompanied by changes in positronium components, the result may be distorted due to inaccuracies in the model used for spectral analysis. Therefore, the validity of the change in non-Ps positron lifetime is difficult to interpret when positronium is formed in the samples.

However, more reliable information about non-Ps positron annihilation sites can be obtained with CDB. Differences in CDB results between **Fresh-dry air 120 °C-hydr** and **Fresh-dry vac 120 °C-hydr** (Fig.10) reflect changes in the non-Ps positron annihilation sites with a minor contribution from positronium (in both cases ca. 20% from o-Ps and 10% from p-Ps). To amplify the differences, the ratio curves from samples with different treatments are compared to the curves obtained for the main components of MS13X, i.e., silicon and aluminum oxides, represented by quartz and sapphire, respectively. In Fig.10, all annihilation radiation lines are relative to the line obtained for quartz (a) or for **Fresh-dry vac 120 °C-hydr** (b).

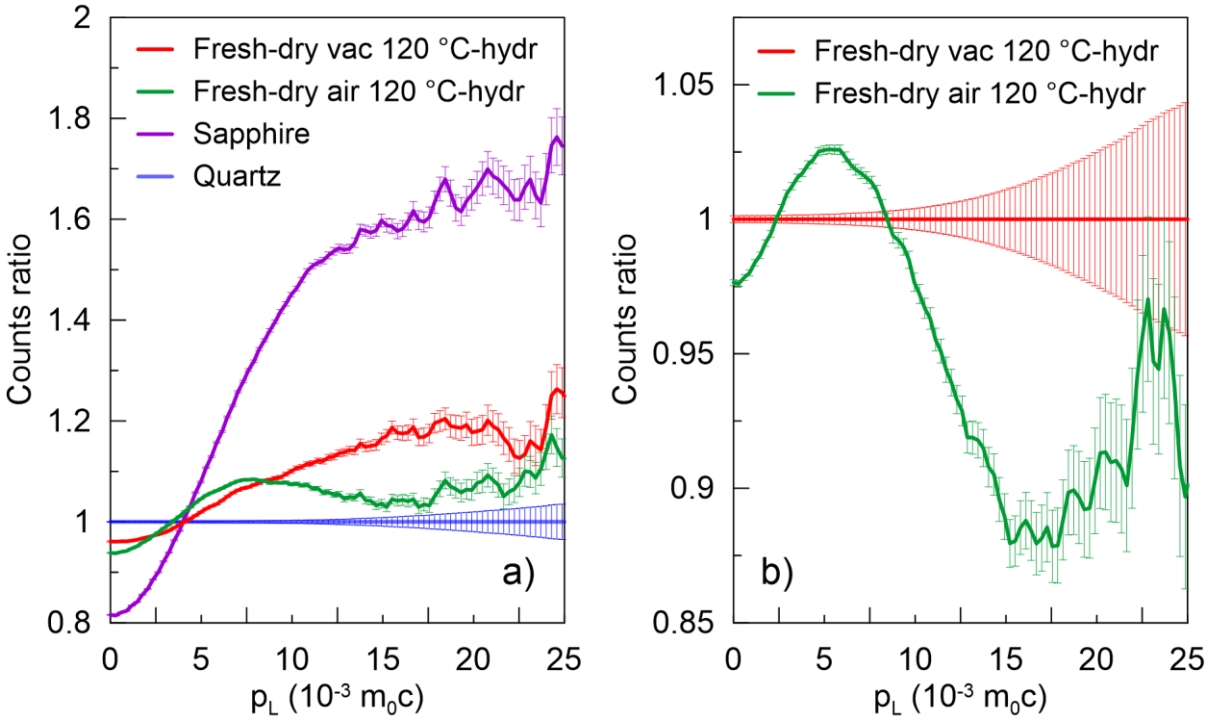

Fig.10. Ratio curves related to Quartz (a) or vacuum-dried MS13X (b) for the coincidence Doppler broadening spectra of MS13X samples **Fresh-dry vac 120 °C-hydr** and **Fresh-dry air 120 °C-hydr**, as well as reference SiO_2 (Quartz) and Al_2O_3 (Sapphire).

The CDB ratio curve for the **Fresh-dry vac 120 °C-hydr** curve is a combination of sapphire and quartz curves (as indicated by its shape and intersection point). The ratio of the contributions of quartz and sapphire curves to **Fresh-dry vac 120 °C-hydr** is closer to the Si:Al ratio of 3:1 observed with XPS than obtained with EDX. This suggests that positrons are trapped mainly on the MS13X surface, with a significant fraction of positrons being trapped in the binder since that is where the XPS data comes from. On the contrary, the ratio curve for **Fresh-dry air 120 °C-hydr** has a significant addition of momenta from a different

element, which gives a contribution to electron momenta in the range of 3-8×10^{-3} m_0c. This suggests that positron traps near another element that is present in the sample are formed. Such an element with a high concentration that usually repels positrons due to its positive charge can be Na^+. This occurs when the Na^+ charge is polarized because of the interaction of the Na ion with a water molecule.

4. Conclusions

In-depth studies of commercial-grade zeolites and their response to environmental changes are necessary to improve their efficiency. MS13X samples were measured using SEM, EDX, and XPS to, among other things, better understand the quantity and location of the binder used to form the zeolite powder into beads. Microscopic images (via SEM) and elemental composition (*via* EDX and XPS) of MS13X beads revealed that the binder was present throughout the interior of the beads but predominated in their outer layer. However, the binder does not seem to interfere with the adsorption capabilities of zeolites significantly. Further PALS studies showed that the amount of free volume is negligible in the fully hydrated zeolite. This indicates that the binder does not block water access to the zeolite cages, because if a significant amount of them were not filled with water, it would be detected by positron porosimetry, which is sensitive to closed pores.

Changes in free volumes during water adsorption and desorption can be observed with PALS with high accuracy. Specifically, PALS can determine the sizes and relative concentrations of free volumes in zeolites at various hydration levels with an uncertainty of less than a few percent. This facilitates a detailed reconstruction of processes leading to the filling of supercages, sodalite cages, and other groups of free volumes with water. Even sodalite cages and Ps bubbles in water, which are comparable in size, can be distinguished from each other by considering the changes in o-Ps intensity that occur throughout the water adsorption and desorption processes. However, to properly understand the PALS results in such a complex system as MS13X, a knowledge of the phenomena accompanying the creation and annihilation of Ps, such as bubble formation and Ps migration between pores of different sizes, is indispensable.

While analyzing the lifetime spectrum of fresh MS13X, unexpected components were discovered whose lifetimes correspond to free volumes of 1-3 nm in size. However, it was concluded that these components were likely to originate from o-Ps chemically binding to pore surfaces, with $PsNa^+$ being in the molecular complex form. Attempts to understand the origin of these components led to the discovery of changes in the hydration state of the sample after different treatments. Hydrated samples dried in the air at 120 °C had significantly more water trapped in MS13X compared to hydrated samples dried in a vacuum at 120 °C, even after pumping at just room temperature (which, however, takes dozens of hours). PALS and CDB analysis indicate that the remaining water molecules were in the vicinity of Na^+ ions. The unexpected components vanished when the samples were hydrated and did not return once the samples were dehydrated, except for water molecules strongly bound to Na^+. This is further evidence that Ps bonded with Na^+ ions, which could not happen if Na^+ was blocked by water.

In addition, PALS was capable of monitoring changes in the adsorption and desorption processes on a time scale of several minutes. The speed of the changes due to MS13X hydration and drying depended mainly on drying conditions, but also on prior treatment of the sample. For example, it was demonstrated that two relatively fast processes occur when samples are dried in a vacuum at 120 °C, compared to only one slower process at 20 °C or 60 °C. Furthermore, it appears that only the faster of the desorption processes occurs when

drying the samples in the air, implying the process is similar to a sub-nanometer-version of evaporation and boiling, where interaction with the material surface prevails. This research paves the way for further studies such as:

- Investigation of the drying course of MS13X and its effects at different temperatures and in controlled atmospheres, e.g., at different oxygen or nitrogen pressures.
- Expansion of CDB research with studies at different hydration states and in different stages of drying.
- Observation of how the interval between water absorption and water desorption affects the desorption process and final state of the sample.

Data Availability Statement

Data will be made available on request.

Declaration of competing interest

The authors declare that they have no known competing financial interests or personal relationships that could have appeared to influence the work reported in this paper.

CRediT authorship contribution statement

Radosław Zaleski: Supervision, Project administration, Writing – original draft, Conceptualization, Formal analysis, Investigation, Writing – review & editing. George Evans: Investigation, Writing – review & editing. Agnieszka Kierys: Writing – original draft, Conceptualization, Formal analysis, Investigation, Writing – review & editing. Mateusz Kochel: Writing – original draft, Conceptualization, Writing – review & editing. Marcin Kuśmierz: Investigation, Formal analysis. Jagoda Urban-Klaehn: Investigation, Writing – review & editing. Robert Staub: Investigation, Writing – original draft. Marek Wiertel: Investigation, Writing – original draft.

Received: ((will be filled in by the editorial staff))
Revised: ((will be filled in by the editorial staff))
Published online: ((will be filled in by the editorial staff))

References

[1] P. C. Wankat, *Separation Process Engineering*, Pearson Education, **2006**.
[2] K. Gleichmann, B. Unger, A. Brandt, in *Zeolites - Useful Minerals* (Ed.: C. Belviso), InTech, **2016**.
[3] B. Unger, K. Schumann, A. Brandt, *Chem. Ing. Tech.* **2010**, *82*, 929-940.
[4] J. Pérez-Pellitero, G. D. Pirngruber, in *New Developments in Adsorption/Separation of Small Molecules by Zeolites, Vol. 184* (Eds.: S. Valencia, F. Rey), Springer International Publishing, Cham, **2020**, pp. 195-225.
[5] C. Baerlocher, D. Brouwer, B. Marler, L. B. McCusker*, Vol. 2024*, **2024**.
[6] P. Azhagapillai, M. Khaleel, F. Zoghieb, G. Luckachan, L. Jacob, D. Reinalda, *ACS Omega* **2022**, *7*, 6463-6471.
[7] K. N. Son, T.-M. J. Richardson, G. E. Cmarik, *J. Chem. Eng. Data* **2019**, *64*, 1063-1071.
[8] P. Aa, *Progress in Petrochemical Science* **2018**, *2*, 1-3.
[9] X. Chen, G. Liu, W. Jin, *Green Energy & Environment* **2021**, *6*, 176-192.
[10] A. Arefi Pour, S. Sharifnia, R. Neishabori Salehi, M. Ghodrati, *Journal of Natural Gas Science and Engineering* **2016**, *36*, 630-643.
[11] T. D. Pham, M. R. Hudson, C. M. Brown, R. F. Lobo, *ChemSusChem* **2017**, *10*, 946-957.
[12] Z. Liu, C. Shen, F. V. S. Lopes, P. Li, J. Yu, C. A. Grande, A. E. Rodrigues, *Sep. Sci. Technol.* **2013**, *48*, 388-402.
[13] T. Montanari, E. Finocchio, E. Salvatore, G. Garuti, A. Giordano, C. Pistarino, G. Busca, *Energy* **2011**, *36*, 314-319.
[14] G. ORTIZ, Q. Persillon, Arkema France SA, **2022**.
[15] J. C. Santos, F. D. Magalhães, A. Mendes, *Ind. Eng. Chem. Res.* **2008**, *47*, 6197-6203.
[16] F. Ambrosino, N. Gargiulo, G. D. Peruta, C. Gravino, G. Gagliardo, F. Pisciotta, S. Esposito, G. La Verde, D. Caputo, M. Pugliese, *Journal of Hazardous Materials Advances* **2024**, *16*, 100458.
[17] T. C. Golden, M. A. Kalbassi, C. J. Raiswell, C. Waweru, M. Pollock, Air Products and Chemicals Inc, **2018**.
[18] F. E. Epiepang, J. Li, Y. Liu, R. T. Yang, *Chem. Eng. Sci.* **2016**, *147*, 100-108.
[19] A. Brandt, J. Schmeisser, B. Unger, H. Tschritter, U. Henkel, G. Bálint, D. Gruhle, G. Winterstein, Chemiewerk Bad Kostritz GmbH, **2017**.
[20] Y. Yang, N. Burke, J. Zhang, S. Huang, S. Lim, Y. Zhu, *RSC Advances* **2014**, *4*, 7279.
[21] T. Ogawa, K. Iyoki, T. Fukushima, Y. Kajikawa, *Materials* **2017**, *10*, 1428.
[22] L. Lakiss, J.-P. Gilson, V. Valtchev, S. Mintova, A. Vicente, A. Vimont, R. Bedard, S. Abdo, J. Bricker, *Microporous Mesoporous Mater.* **2020**, *299*, 110114.
[23] R. Bingre, B. Louis, P. Nguyen, *Catalysts* **2018**, *8*, 163.
[24] A. Pfenninger, in *Structures and Structure Determination, Vol. 2* (Eds.: C. Baerlocher, J. M. Bennett, W. Depmeier, A. N. Fitch, H. Jobic, H. Van Koningsveld, W. M. Meier, A. Pfenninger, O. Terasaki), Springer Berlin Heidelberg, Berlin, Heidelberg, **1999**, pp. 163-198.
[25] W. Vermeiren, J.-P. Gilson, *Top. Catal.* **2009**, *52*, 1131-1161.
[26] L. García, G. Rodríguez, A. Orjuela, *Brazilian Journal of Chemical Engineering* **2021**, *38*, 165-175.
[27] P. S. F. Mendes, J. M. Silva, M. F. Ribeiro, A. Daudin, C. Bouchy, *Journal of Industrial and Engineering Chemistry* **2018**, *62*, 72-83.
[28] M. Król, A. Mikuła, *Microporous Mesoporous Mater.* **2017**, *243*, 201-205.

[29] J. Jänchen, A. Brandt, B. Unger, J. Schmeißer, H. Stach, U. Hellwig, in *EuroSun 2010*, International Solar Energy Society, **2010**, pp. 1-8.
[30] F. Akhtar, L. Andersson, S. Ogunwumi, N. Hedin, L. Bergström, *J. Eur. Ceram. Soc.* **2014**, *34*, 1643-1666.
[31] M. Hartmann, M. Thommes, W. Schwieger, *Advanced Materials Interfaces* **2021**, *8*, 2001841.
[32] N.-L. Michels, S. Mitchell, J. Pérez-Ramírez, *ACS Catalysis* **2014**, *4*, 2409-2417.
[33] K. Schumann, B. Unger, A. Brandt, F. Scheffler, *Microporous Mesoporous Mater.* **2012**, *154*, 119-123.
[34] M. Thommes, K. Kaneko, V. Neimark Alexander, P. Olivier James, F. Rodriguez-Reinoso, J. Rouquerol, S. W. Sing Kenneth, in *Pure Appl. Chem., Vol. 87*, **2015**, p. 1051.
[35] K. Chen, S. H. Mousavi, R. Singh, R. Q. Snurr, G. Li, P. A. Webley, *Chem. Soc. Rev.* **2022**, *51*, 1139-1166.
[36] J. Shang, G. Li, R. Singh, Q. Gu, K. M. Nairn, T. J. Bastow, N. Medhekar, C. M. Doherty, A. J. Hill, J. Z. Liu, P. A. Webley, *J. Am. Chem. Soc.* **2012**, *134*, 19246-19253.
[37] R. Zaleski, *Nukleonika* **2015**, *60*, 795-800.
[38] A. G. Attallah, V. Bon, K. Maity, R. Zaleski, E. Hirschmann, S. Kaskel, A. Wagner, *The Journal of Physical Chemistry Letters* **2024**, *15*, 4560-4567.
[39] T. Stassin, R. Verbeke, A. J. Cruz, S. Rodríguez-Hermida, I. Stassen, J. Marreiros, M. Krishtab, M. Dickmann, W. Egger, I. F. J. Vankelecom, S. Furukawa, D. De Vos, D. Grosso, M. Thommes, R. Ameloot, *Adv. Mater.* **2021**, *33*, 2006993.
[40] A. G. Attallah, V. Bon, K. Maity, E. Hirschmann, M. Butterling, A. Wagner, S. Kaskel, *ACS Applied Materials & Interfaces* **2023**, *15*, 48264-48276.
[41] A. Zubiaga, R. Warringham, S. Mitchell, L. Gerchow, D. Cooke, P. Crivelli, J. Pérez‐Ramírez, *ChemPhysChem* **2017**, *18*, 470-479.
[42] R. Warringham, L. Gerchow, A. Zubiaga, D. Cooke, P. Crivelli, S. Mitchell, J. Pérez-Ramírez, *The Journal of Physical Chemistry C* **2016**, *120*, 25451-25461.
[43] A. Cabral-Prieto, I. García-Sosa, R. López-Castañares, O. Olea-Cardoso, *Microporous Mesoporous Mater.* **2013**, *175*, 134-140.
[44] J. Urban-Klaehn, K. Shikhaliyev, A. Gaffney, A. Martinez, R. Zaleski, J. Lauterbach, A. Katz, A. Jaeshke, X. Li, *ChemCatChem* **2024**, *16*, e202301282.
[45] M. Milina, S. Mitchell, D. Cooke, P. Crivelli, J. Pérez‐Ramírez, *Angewandte Chemie International Edition* **2015**, *54*, 1591-1594.
[46] R. Zaleski, A. Kierys, M. Pietrow, B. Zgardzińska, A. Błażewicz, *J. Colloid Interface Sci.* **2020**, *558*, 259-268.
[47] P. Maheshwari, M. Gorgol, A. Kierys, R. Zaleski, *J. Phys. Chem. C* **2017**, *121*, 17251-17262.
[48] V. T. Adonkin, B. M. Gorelov, D. V. Morozovskay, V. M. Ogenko, *Colloids and Surfaces A: Physicochemical and Engineering Aspects* **1995**, *101*, 233-237.
[49] S. Brunauer, P. H. Emmett, E. Teller, *J. Am. Chem. Soc.* **1938**, *60*, 309-319.
[50] F. Bečvář, J. Čížek, I. Procházka, *Appl. Surf. Sci.* **2008**, *255*, 111-114.
[51] J. Kansy, *Nucl. Instrum. Methods Phys. Res., Sect. A* **1996**, *374*, 235-244.
[52] A. Shukla, M. Peter, L. Hoffmann, *Nucl. Instrum. Methods Phys. Res., Sect. A* **1993**, *335*, 310-317.
[53] C. N. Taylor, T. F. Fuerst, M. Shimada, *AIP Conf. Proc.* **2019**, *2182*.
[54] G. S. Evans, J. M. Watkins, C. N. Taylor, J. Urban-Klaehn, C. T. Tsai, *SoftwareX* **2023**, *23*, 101475.
[55] J. Goworek, R. Zaleski, W. Buda, A. Kierys, *Appl. Surf. Sci.* **2010**, *256*, 5316-5322.

[56] R. Zaleski, W. Dolecki, A. Kierys, J. Goworek, *Microporous Mesoporous Mater.* **2012**, *154*, 142-147.
[57] R. Zaleski, A. Kierys, M. Gorgol, *Phys. Chem. Chem. Phys.* **2017**, *19*, 10009-10019.
[58] R. Zaleski, P. Krasucka, K. Skrzypiec, J. Goworek, *Macromolecules* **2017**, *50*, 5080-5089.
[59] R. Zaleski, W. Stefaniak, J. Goworek, *Experimental Thermal and Fluid Science* **2021**, *128*, 110435.
[60] R. Zaleski, M. Gorgol, A. Kierys, P. Maheshwari, M. Pietrow, P. K. Pujari, B. Zgardzińska, *The Journal of Physical Chemistry C* **2022**, *126*, 5916-5926.
[61] R. Zaleski, A. Błażewicz, A. Kierys, *Nukleonika* **2013**, *58*, 233−238.
[62] R. A. Ferrell, *Phys. Rev.* **1957**, *108*, 167-168.
[63] R. Zaleski, O. Kotowicz, A. Górska, K. Zaleski, B. Zgardzińska, *The Journal of Physical Chemistry B* **2023**, *127*, 9887-9890.
[64] M. Thangswamy, D. Dutta, P. Maheshwari, D. Sen, P. K. Pujari, *Phys. Chem. Chem. Phys.* **2019**, *21*, 6033-6041.
[65] K. Ito, S. Yoshimoto, B. E. O'Rourke, N. Oshima, K. Kumagai, *Appl. Phys. Lett.* **2018**, *112*, 083701.
[66] P. Maheshwari, D. Dutta, T. Muthulakshmi, B. Chakraborty, N. Raje, P. K. Pujari, *J. Phys.: Condens. Matter* **2016**, *29*, 055003.
[67] H. Klym, A. Ingram, O. Shpotyuk, I. Hadzaman, V. Solntsev, *Nanoscale Research Letters* **2016**, *11*, 1-7.
[68] O. Šauša, I. Mat'ko, E. Illeková, E. Macová, D. Berek, *Journal of Physics: Conference Series* **2015**, *618*, 012041.
[69] I. Matko, O. Sausa, E. Macova, D. Berek, *J. Therm. Anal. Calorim.* **2015**, *121*, 163-168.
[70] M. Roussenova, M. A. Alam, S. Townrow, D. Kilburn, P. E. Sokol, R. Guillet-Nicolas, F. Kleitz, *New Journal of Physics* **2014**, *16*, 103030.
[71] P. Maheshwari, P. K. Pujari, S. K. Sharma, D. Dutta, K. Sudarshan, V. S. Mithu, P. K. Madhu, S. K. Deshpande, P. N. Patil, N. Raje, *The Journal of Physical Chemistry C* **2013**, *117*, 14313-14324.
[72] M. Gorgol, R. Zaleski, A. Kierys, *Nukleonika* **2013**, *58*, 227−231.
[73] F. Ucun, *Zeitschrift für Naturforschung A* **2002**, *57*, 281-282.
[74] J. H. Hack, Y. Chen, N. H. C. Lewis, H. H. Kung, A. Tokmakoff, *The Journal of Physical Chemistry B* **2023**, *127*, 11054-11063.
[75] C. Abrioux, B. Coasne, G. Maurin, F. Henn, M. Jeffroy, A. Boutin, *The Journal of Physical Chemistry C* **2009**, *113*, 10696-10705.
[76] Y. Kobayashi, *Chem. Phys. Lett.* **1991**, *182*, 440-444.
[77] D. M. Schrader, *Nucl. Instrum. Methods Phys. Res., Sect. B* **1998**, *143*, 209-217.
[78] J. Usukura, K. Varga, Y. Suzuki, *Phys. Rev. A* **1998**, *58*, 1918-1931.
[79] J. Mitroy, M. W. J. Bromley, G. G. Ryzhikh, *J. Phys. B: At., Mol. Opt. Phys.* **2002**, *35*, R81.

Supporting Information

Supporting Information is available from the Wiley Online Library or from the author.

This study addresses a research gap regarding commercially available zeolites. Positron annihilation lifetime spectroscopy (PALS) is applied to determine the size and concentration of water-free volumes at various hydration levels and to monitor minute-scale adsorption and desorption dynamics. The bead binder does not block water access to zeolite cages, and in air-dried samples, water molecules remain near Na^+ ions.

ToC figure